Proceedings of ASME Turbo Expo 2011
GT2011
June 6-10, 2011, Vancouver, British Columbia, Canada

GT2011-46455

IMPACT OF A COLLECTOR BOX ON THE PRESSURE RECOVERY OF AN EXHAUST DIFFUSER SYSTEM

Bryan C. Bernier,
Mark Ricklick, J. S. Kapat
Center for Advanced Turbines and Energy Research
Laboratory for Turbine Aerodynamics, Heat Transfer, and Durability
University of Central Florida
Orlando, FL, 32816

ABSTRACT

The effects of an industrial gas turbine's Exhaust Collector Box (ECB) geometry on static pressure recovery and total pressure loss were investigated in this study. This study aims to further understand how exit boundary conditions affect the performance of a diffuser system. In this investigation, the exhaust diffuser remained constant through each test, with collector box geometries being varied. The same uniform velocity profile was maintained at the diffuser inlet for all geometries considered. The local pressure recovery through the diffuser with 4 axial ports at 4 circumferential locations was reported along with 14 locations in the accompanying ECB. A system performance analysis for each geometry was conducted using the total pressure loss from inlet to exit of the model. Velocity and total pressure profiles obtained with a hotwire anemometer and Kiel probe at the exit of the diffuser and at the exit of the ECB are also presented in this study. Three (3) different ECB geometries are investigated at a Reynolds number of 60,000. Results obtained from these experimental tests are used to validate the accuracy of a 3-dimensional RANS with realizable k-ε turbulence CFD model from the commercial software package Star-CCM+. The study confirms the existence of two strong counter-rotating helical vortices at the exit of the ECB which significantly affect the flow within the diffuser. Evidence of a strong recirculation zone within the ECB was found to force separation within the exhaust diffuser. Extending the length of the ECB proved to decrease the total pressure loss of the system by up to 19% experimentally. Additionally, the realizable k-ε turbulence was able to accurately represent the total pressure loss of the system within 5%. Despite the extremely complex flow field within the ECB, the computational domain reasonably represented the system in both magnitude and trends.

NOMENCLATURE

M	Mach Number
e/D_h	Relative Surface Roughness
SCFM	Standard Cubic Feet per Minute
D_h	Hydraulic Diameter
L	ECB Length
W	ECB Width
H	ECB Height
Re	Reynolds Number ($\rho V_0 D_h/\mu$)
P	Static Pressure
P_0	Total Pressure
Cp	Pressure Recovery Coefficient
X	Local Axial Location
L	Diffuser Axial Length
Dp	Smooth Pipe Diameter
Vb	Bulk Velocity
R_o	Outer Radius
R_i	Inner Radius
V	Velocity
Vx	Axial Velocity
V_0	Average Diffuser Inlet Velocity
TI	Turbulence Intensity
TI_{avg}	Local Average Turbulence Intensity

INTRODUCTION

The purpose of this gas turbine exhaust diffuser is to recover as much dynamic head as possible before the flow exits into the atmosphere, increasing the static pressure with minimum total pressure losses. This enables the turbine stage to experience a higher pressure ratio than it would if there was no

exit diffuser, thus increasing the amount of work extracted by the turbine stages. The flow in this exhaust diffuser is still moving at a speed where the dynamic head is not negligible, thus a significant amount of static pressure could possibly be recovered through an efficient diffuser design. In the land based power generation turbines, or marine based propulsion turbines, the engine may be enclosed in a structure which requires proper ventilation of the exhaust gasses. The need for proper ventilation also occurs in vehicles such as tanks and helicopters. The combination of the need for pressure recovery and the limited enclosed space is where the exhaust collector box (ECB) comes into the picture.

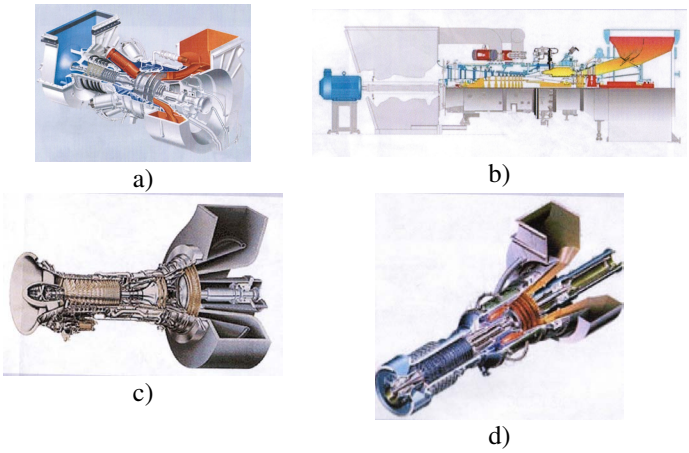

Figure 1 – Variations in the Industrial gas turbine exhaust diffuser collector box. A) SGT-700, b) SGT-600, C) Dresser-Rand DR-61, D) Solar-Mars Gas Turbine

In most cases, the exhaust gasses are directed upwards and out of the structure. The addition of this exhaust collector box is a necessary section in some turbines, however it does increase the total pressure loss of the system by adding additional ducting and turns to the flow path. The wide variation in industrial designs for the diffuser exhaust collector box design is depicted in the various designs in Figure 1. While every design is different, the ultimate goal of the exhaust system is equivalent in every engine. The fundamental aspects of diffuser performance (sensitive to inlet profile, separation, etc.) are also common for every exhaust system. The goal of this study is to look at the flow structures within an exhaust system to gain some knowledge of what factors go into the pressure recovery and total pressure loss, and hopefully find ways to improve the performance. If the exhaust could be vented away in an efficient manner, the system performance could increase thus generating more power and reducing specific fuel consumption. In this study, we investigate the design of the exhaust collector box downstream of the engine's final diffuser and how it affects the system performance.

A three stage entraining diffuser was studied in [1] with a distorted inlet flow. Two different circular to slot transition ducts with a 90 degree bend were used with varying inlet swirl. Significant impingement effects were observed on the back wall of the transition ducts, while flow reversal and separation was observed on the front wall. These effects were dampened by the introduction of swirl to the inlet, however the secondary flows were intensified. The swirl also intensified the velocity distortion at the diffuser inlet. A scaled down model of the PGT10 gas turbine exhaust diffuser was investigated in [2]. Static pressure measurements taken axially along the strut axis, showing significant stagnation on the shroud and a slight stagnation on the hub at the leading edge of the struts. Both the hub and shroud pressures converged after the struts and at the diffuser exit. The diffuser performance was slightly higher for the geometry with no struts, concluding that the struts introduce a local reduction in area causing the flow to potentially have a higher pressure gradient downstream. A scaled model of the GE-MS9001E gas turbine exhaust system was studied by [3] both experimentally and computationally under multiple loading conditions. Experimental data was taken in between the struts, at strut outlet plane, and model outlet plane and compared with a 3-dimensional RANS method with the standard high-Reynolds-number k-e turbulence model. This study is similar to the present study, however the main focus of the former was on the flow patterns within the diffuser with very little data on the exhaust stack. A single geometry was studied while the loading condition (inlet velocity profile) was varied. The total and static pressure losses were derived from the measurements, and were determined to be slightly higher than the computational results, concluding in the fact that the computation does not fully capture the secondary flow losses in the turning vanes. Overall, the computational model was a successful design tool which reasonably predicts the performance of a complex exhaust system. More recently, in 2010 a study was performed by [4] investigating the effect of the total pressure inlet profile on the performance of an axial diffuser. The geometry of their diffuser is similar to the present study, however it lacks the exhaust collector box. Their study also shows the weakness of the computational models, as they are inaccurately capturing the effect of separation and flow reversal. This study aims to look further into the flow structures within the exhaust collector box and why these structures have a detrimental affect the diffuser performance.

EXPERIMENTAL SETUP

The overall goal of the flow conditioning was to create a uniform velocity profile at the inlet of the diffuser as diffusers are incredibly sensitive to any variations in the inlet velocity profile[3-13]. A series of flow conditioning devices were installed into a large upstream plenum, and were designed to generate a uniform velocity profile at the exit of the nozzle. Once the flow exits the plenum, it is contracted by an annular nozzle. The nozzle has a contraction ratio of 4.6 and is designed based on [14]. The diffuser was removed for inlet velocity measurements, leaving the nozzle exhausting into the atmosphere.

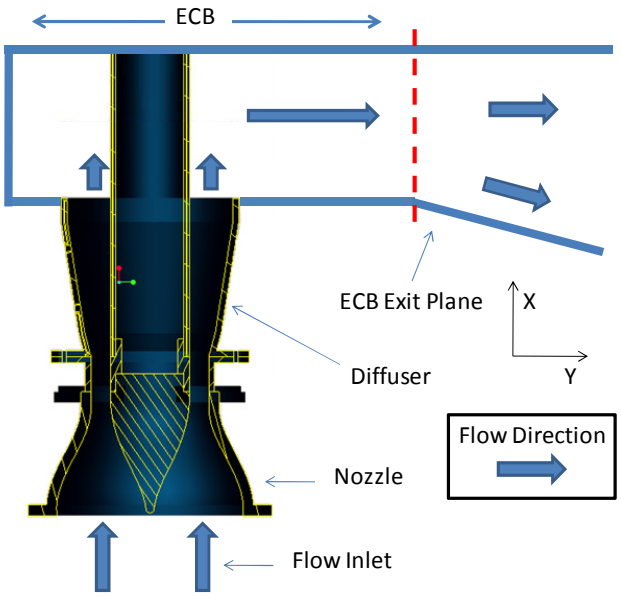

Figure 2 – Experimental rig setup

The circumferential total pressure profile at the exit of the nozzle is shown in Figure 3 with a free exit condition. The total pressure at the nozzle exit did not vary by more than 2% circumferentially, giving confidence to the uniform velocity profile at the diffuser inlet. The experiments were conducted using the pressure side of a Spencer VB110 Vortex Regenerative Blower capable of supply up to 600 SCFM of air at approximately 310K. Due to the low Mach numbers (M < 0.2), the flow is considered incompressible in the entire study.

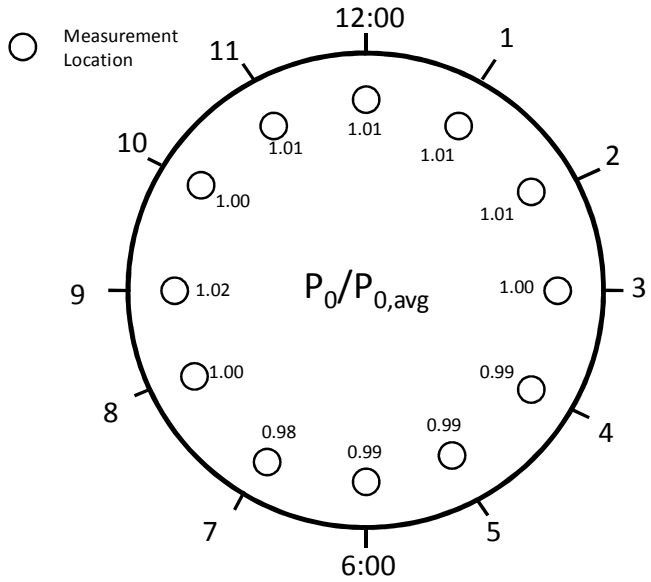

Figure 3 – Circumferential nozzle exit total pressure (normalized by the local average total pressure) profile with a free exit condition (no diffuser)

The operating flow rate was measured and controlled using a Low-Loss Preso CV Venturi upstream of the plenum.

The small scale diffuser was created using rapid prototyping technology. The inlet e/D_h of the diffuser is 0.0002, which when combined with the operating Reynolds number of 60,000, gives a Darcy-Weisbach friction factor of 0.022 which is close to a smooth wall. The diffuser has an area ratio of 2.8 and is outfitted with numerous pressure ports.

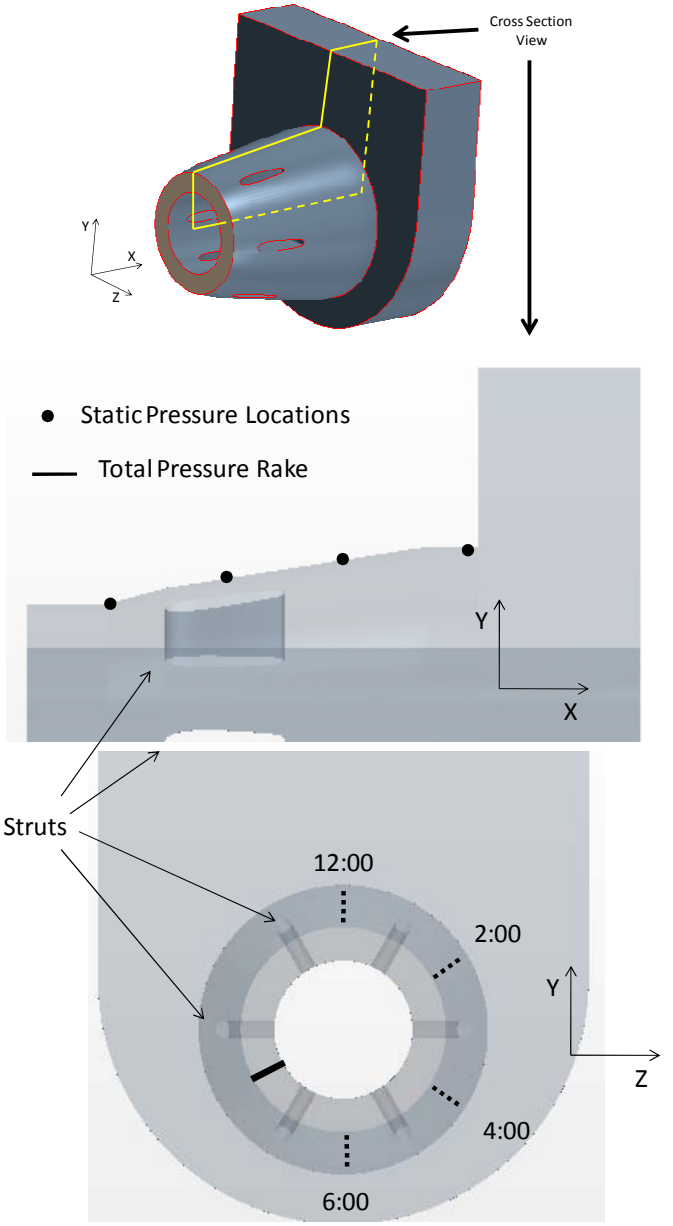

Figure 4 – Cross sectional plane (top) of the diffuser system showing axial positions of static pressure ports (mid) and Circumferential locations of pressure ports and total pressure rake (bottom).

There are pressure taps at four axial positions (0%, 33%, 66%, 100% of total length) and four circumferential positions (12:00, 2:00, 4:00, 6:00) giving 16 ports evenly spaced around one half of the diffuser circumference. This is illustrated in Figure 4. A total pressure rake consisting of 3

probes (probe head diameter < 3% of D_h) were permanently placed upstream of the diffuser inlet at the 8:00 location spaced evenly between the inner and outer radius. The average of these three probes was used as the reference inlet total pressure (typical variation of less than 5%). The ECB investigated in this study is shown in Figure 5. For computational reasons, the exit duct has been extended to alleviate any flow distortions due to exit boundary conditions; however the measurement plane is at the same location as on the experimental rig.

Investigated Geometries

There are three major dimensions of the ECB: height, width, and length. The width is defined as the distance (in the Z direction) from wall to wall in the collector box, the length is defined as the distance (in the X direction) from the diffuser exit to the back wall of the collector box, and the height (or 6'oclock height) is defined as the distance from the diffuser exit to the bottom of the collector box (in the Y direction). Each case was tested at a Re = 60,000 calculated at the diffuser inlet, using the inlet hydraulic diameter. Figure 5 and Table 1 describes these dimensions for each of the three cases tested. For each case investigated, the hydraulic diameter remained constant while the length of the ECB was increased by 50%, and 100% for Case 2 and 3 respectively. The width and height of the ECB also remained constant in this study.

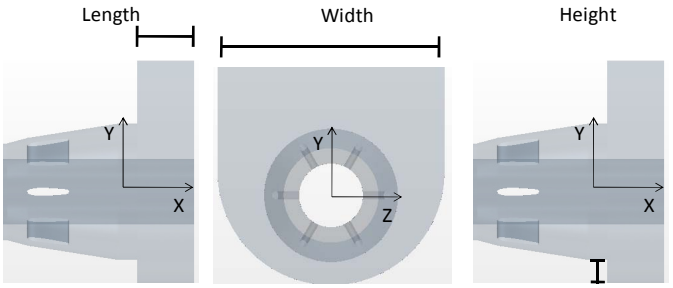

Figure 5 – Geometric variables: Length (left), Width (center) and Height (right) of the exhaust collector box study.

Table 1 – ECB Geometries

Geometry	Changes	H/Dh	W/Dh	L/Dh
Case 1	-----	.75	7.4	1.8
Case 2	+50% Length	.75	7.4	2.7
Case 3	+100% Length	.75	7.4	3.6

Data Reduction and Uncertainty

The data obtained from this experiment has been reduced into non-dimensional quantities so that the experiment can easily be scaled for design considerations. For the diffuser and ECB performance, the static pressure recovery coefficient, Cp is used. The definition for Cp at any given location, (x), is shown in Equation 1.

$$C_{p_x} = \frac{P_x - P_1}{P_{01} - P_1} \quad (1)$$

For this experiment, the reference values (P_1, P_{01}) are taken at the inlet of the diffuser. Three total pressure probes are permanently placed at the 8:00 location (shown in Figure 4) between the nozzle and the diffuser to measure the inlet total pressure. The reference static pressure is taken as the average of the X/L = 0% ports along the 12:00, 2:00, 4:00, and 6:00 planes. Typical variations in these ports were on the order of +/- 20% of the average gage static pressure. The ECB exit plane total pressure profiles were measured using a Kiel probe with diameter of less than 5% of the ECB Height. The Kiel probe was calibrated to read the total pressure accurately for a +/- 50° cone angle. This probe was traversed along the exit plane of the ECB for a total of 72 measurement locations (12 locations along the width, 6 locations along the height).

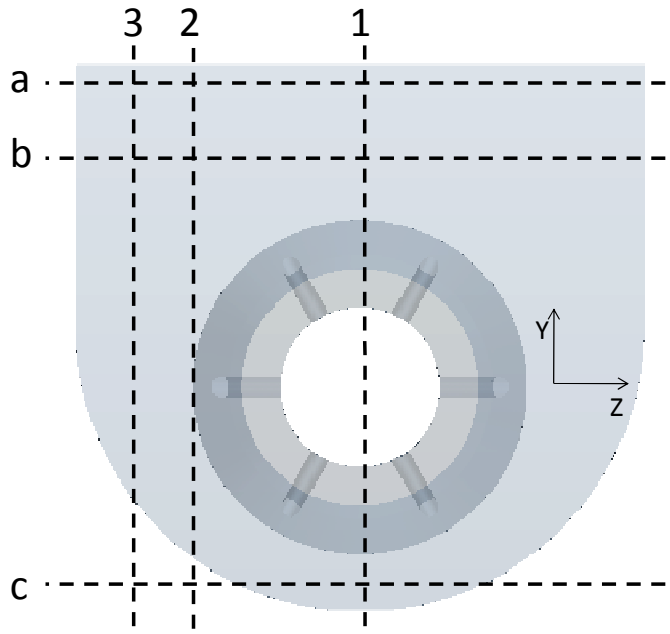

Figure 6 – Coordinate system definition of static pressure port locations on the ECB. Planes 1, 2, and 3 vary in the Z-axis while planes a, b, and c vary the Y-axis.

Diffuser inlet and exit velocity profiles were measured using a constant temperature hotwire anemometer placed on a traversing system. The hotwire wire diameter was less than 0.02% of the hydraulic diameter of the diffuser. The inlet profile was measured at the 6:00 location, and the exit profile was measured at 6:00 (between struts) and 5:00 (behind a strut) at the exit of the diffuser. The ECB was also investigated in this study in a variety of ways. An array of static pressure ports was placed on the ECB to determine the static pressure variations within the collector box. These locations are shown in Figure 6. These ports were placed on the front and back walls of the ECB

in order to study the variations in pressure along the impingement wall (back wall), and the diffuser-side wall (front wall). Data presented on the back wall is denoted with a #' (1a is on the front wall, while 1a' is on the back wall for example). Three measurement planes were taken on the ECB (denoted as 1, 2, and 3 in Figure 6). Plane 1 represents the centerline of the ECB, plane 2 represents the X-Y plane tangent to the outer diameter of the diffuser, and plane 3 represents the X-Y plane located halfway between the outer diameter of the diffuser and the side wall of the ECB. On these planes, static pressure ports were placed at 3 locations along the Y-axis (denoted as a, b, and c).

The performance of the entire system was analyzed using total and static pressure recovery coefficients. The total pressure loss coefficient is defined as follows:

$$\text{Total Pressure Loss Coef.} = (P_{01} - P_{0X}) / (P_{01} - P_1) \qquad (2)$$

Here, P_{0X} is the local average total pressure. The static and total pressures presented are gage pressures with a reference of atmospheric pressure. For the experimental rig, two locations were area averaged for these coefficients; Diffuser inlet and ECB outlet. For the computational model the diffuser inlet, diffuser outlet, and ECB outlet were measured. Two different transducers were used during the experiment. The micro-manometer was used for the individual pressure measurements (such as flow rate monitoring), and for calibration of the Scanivalve transducer. The Scanivalve system is a multiplexing pressure sensor which was used for the majority of the pressure measurements during the test. To reduce noise and small fluctuations 50 measurements were taken at each port over 25 seconds, the average of this set is used in the data reduction.

Table 2 - Uncertainties

	Uncertainty (+/-)
*Scanivalve Pressure	0.9 Pa (<1% of inlet dynamic head)
*Micro-manometer Pressure	0.1 Pa (<0.1% of inlet dynamic head)
Flow Rate	1.1%
Reynolds Number	1.4%
Cp	2.7%

* - Measured Quantities

For this experiment, the uncertainty values can be calculated based on the accuracy of the measurement devices. The uncertainties were calculated as described by [15]. Table 2 describes each measurement and the respective uncertainty.

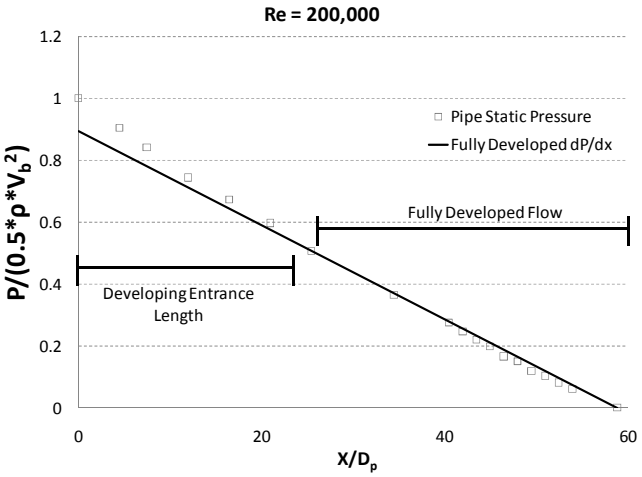

Figure 7 – Smooth pipe validation of the experimental setup. Static pressure normalized by the dynamic head (using bulk velocity, Vb) versus length normalized by the pipe diameter (Dp)

EXPERIMENTAL VALIDATION

To establish confidence in the experimental setup, a smooth pipe friction factor validation case was run. The diffuser and ECB was removed from the system, and replaced with a 60 diameter long smooth pipe instrumented with pressure taps along the wall. Operating at a Reynolds number of 200,000, the friction factor was obtained from [16] giving a fully developed pressure drop as a function of pipe length. This result was plotted against the static pressure along the wall of the smooth pipe and is shown in Figure 7. The developing entrance length is easily distinguished from the data, and the experimental pressure in the fully developed region has a maximum deviation of 2.5% from the data obtained from [16].

COMPUTATIONAL MODEL

The main focus of this study is investigate the accuracy of CFD calculations with today's commercial CFD packages when applied to a diffuser exhaust system. The experimental tests were used as a baseline to compare against the data obtained from the computations. The inlet and exit boundary conditions were matched from the experimental conditions for each case. All data obtained from the computational domain was analyzed at the same physical locations on the diffuser and ECB as the experimental rig. The commercial software StarCCM+ v5.04 [17] was used for the mesh generation and the segregated, steady, incompressible Navier-Stokes solver for this investigation. Figure 8 shows the generated mesh at the 12:00-6:00 cross section, and the strut mid-plane cross section. A grid convergence study was performed over 5 mesh sizes, ranging from 150,000 to 1,200,000 volumes. The different mesh sizes were generated by systematically refining the size of the individual elements in the fluid zones of the model. Figure 9

shows the average total pressure at the exit of the diffuser in Case 1 for all 5 mesh sizes. It was concluded that at a cell count of 750,000 there was no change (<< 1%) in the diffuser exit

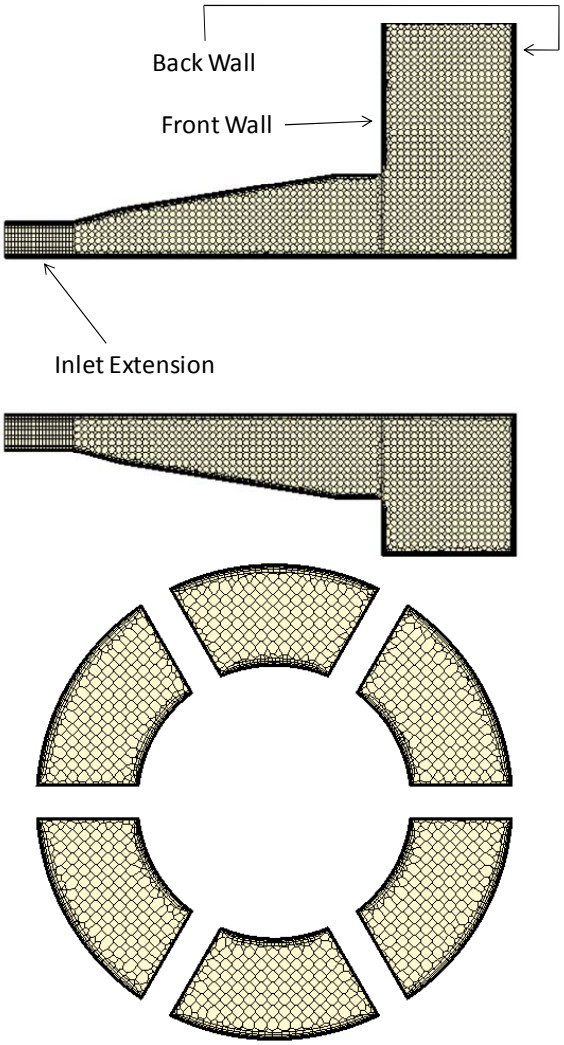

Figure 8– 12:00-6:00 mesh section of the baseline case (top) and the strut mid-chord plane mesh cross section of the baseline case(bottom)

total pressure with an increased number of cells. However, the vortex structures within the ECB require a much finer mesh than the diffuser exit profile, therefore the larger mesh was chosen for all cases in this study. Additionally, the uncertainty in the fine-grid solution was calculated based on [18]. Two data points were chosen for the fine-grid accuracy, the diffuser exit static pressure (taken at X/L=100% at the 12:00 location) and the area averaged total pressure at the exit of the diffuser. These were chosen to define the accuracy in the static pressure recovery, and the total pressure losses through the diffuser. The fine-grid accuracy for the static pressure at the diffuser exit was 1.7% and the total pressure at the diffuser exit was 2.2%.

The final generated mesh for the baseline case contained 1.2 million cells, and wall Y+ values less than 1 in the diffuser and the ECB, and Y+ values greater than 30 in the exit section. Case 2 and 3 contained 1.35 million and 1.5 million cells respectively. Case 2 and 3 contained slightly more cells, however this is only due to the increase in volume as the ECB length was extended. The cell size and surface size of the entire model remained constant through each computational domain.

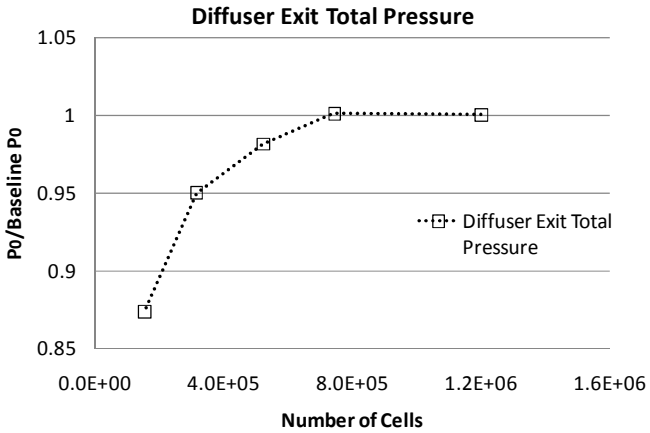

Figure 9 – Grid independence study on the numerical model. Average diffuser exit total pressure is plotted over 5 grid sizes.

An all wall Y+ treatment was used in this model to allow the use of wall cell heights in the diffuser and ECB in the viscous sub-layer (Y+ < 5) and wall cell heights in the exit section in the fully turbulent region (Y+ > 30). The code uses the appropriate wall function depending on the value of Y+. Cells in the intermediate region between these zones are interpolated; however there were only 222 cells (less than 0.015% of total cell count) in this intermediate Y+ region within the diffuser and ECB.

The realizable k-ε model was used in this study with all model constants set as the default values in StarCCM. This model was also used in [3,5,6] under very similar adverse pressure gradient flow fields with successful results. The convergence criteria for the computational model were set at a minimum residual of 10^{-6} for all equations. Iterative convergence was also monitored for the average total pressure at the exit of the diffuser, obtaining convergence when the total pressure change between iterations was less than 10^{-3}. The model convergence was verified when both of these conditions were satisfied. The convergence criteria require approximately 2000 iterations per case.

Three boundary conditions were used in this computational model: In-flow (inlet plane), Out-flow (outlet plane) and No Flow (solid walls). The In-flow condition was set as a constant mass flux, corresponding to the appropriate mass flow through the experimental rig for each case. The boundary layer thickness was approximated by the addition of a straight inlet duct upstream of the diffuser inlet. The length of this duct matched the experimental set up as well. The Out-flow boundary condition was set at atmospheric pressure at the downstream end of an extension duct after the ECB. This Out-

flow condition prescribes the static pressure at every point on the outlet face to be atmospheric pressure. The extension duct was placed downstream of the ECB in order to alleviate any boundary condition effects on the exit of the ECB. The No-flow boundary condition was an adiabatic no-slip condition on all walls within the model.

RESULTS AND DISCUSSION

Diffuser Performance

In order to understand the performance of the diffuser and ECB system, the inlet profile to the system must be well defined. Previous studies have used fully developed inlet conditions [11] however this study investigates a uniform velocity profile at the diffuser inlet. In order to validate our computational model, the ECB was removed from the system, leaving a simple annular diffuser exhausting into the atmosphere. This was done to give access to the exit of the diffuser. During this phase, the inlet and exit velocity profiles were measured with a hotwire anemometer and validated against the computational model with the ECB removed as well. Two traverse locations were chosen at the exit of the diffuser: directly downstream of a strut (7:00), and in-between struts (6:00). These locations were chosen to experimentally define the wake region downstream of the airfoil struts, and compare them to the computational domain. The results for these experiments are shown in Figure 11. The inlet velocity profile was determined to be a flat velocity profile from the experiment and the CFD. The boundary layer thickness was not measured in the experiment. The single hotwire was able to measure the root mean square of the instantaneous axial velocity fluctuations (u_{rms}), thus the turbulent intensities (TI) were calculated. It should be noted that the turbulence quantities obtained assume isotropic turbulence ($u_{rms} = v_{rms} = w_{rms}$) which is not the case at the diffuser exit in this system [19]. Since v_{rms} and w_{rms} are smaller than u_{rms}, the actual turbulent kinetic energy is smaller than the isotropically derived quantity. This causes the experimental data to see higher turbulence than the computational results. On top of this effect, the steady RANS model does not model the oscillating eddies which most likely exist in this system [20]. These eddies can promote turbulent transport through the diffuser. Therefore, the RANS model incorrectly dissipates the turbulence quantities between the struts, causing low turbulence values in this region.. For this reason, the trends of the turbulence (as opposed to the magnitudes) are compared experimentally and computationally by plotting the turbulence intensity (TI) normalized by the local average turbulence intensity (TI_{avg}). Where, TI_{avg} is the average turbulence intensity in the free stream at each measurement location (experimentally and computationally), negating the boundary layer as the experimental data does not extend close to the wall.

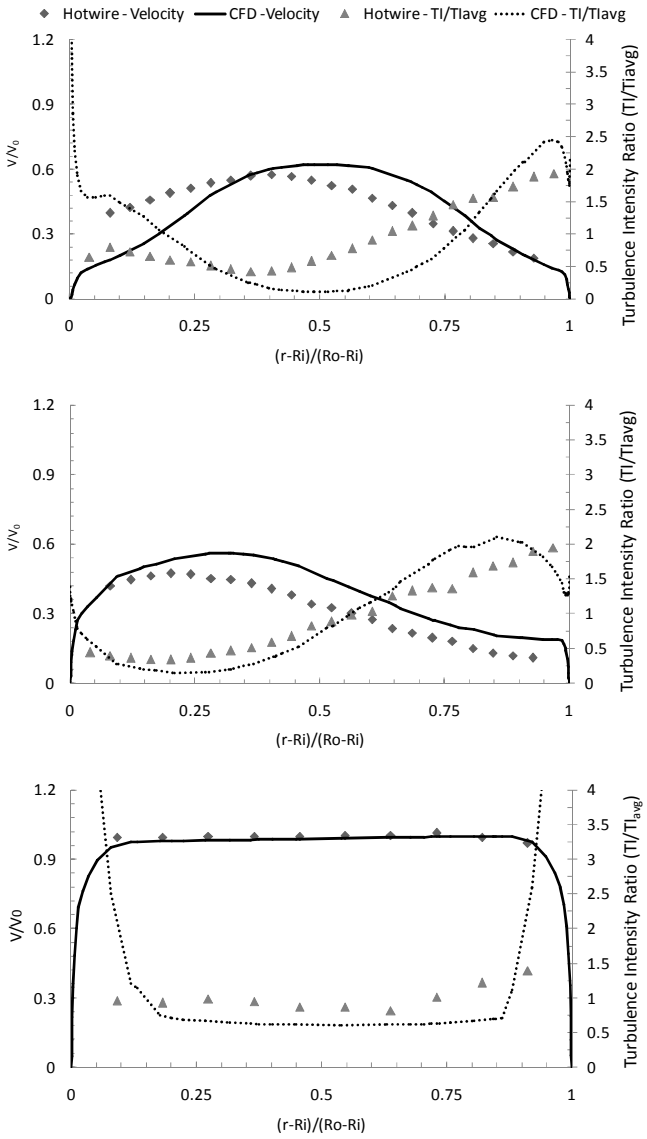

Figure 11 – Experimental and computational results for the velocity profile with no ECB from the ID [(r-Ri)/(Ro-Ri)=0] to OD [(r-Ri)/(Ro-Ri)=1] at the exit between the struts (top), at the exit behind the struts (mid) and at the diffuser inlet (bottom). Velocity is on the left axis, and turbulence intensity ratio is on the right axis.

The average turbulence intensity at each location is presented in Table 3. As expected, the average turbulence intensities measured by a single hotwire are high (nearly double the computational results), however the trends are more accurate. The diffuser inlet conditions (Figure 11 – bottom) are accurate in both magnitude and trends, as the velocity fluctuations are close to isotropic. The computation correctly captured the trend in turbulence directly downstream of a strut (Figure 11 – mid). An under prediction the turbulence in the high velocity region, and an over prediction of turbulence in the low velocity region is seen.

Table 3 – Local average turbulence intensity in the diffuser

	Iavg(%)	
Location	Experiment	Computation
Inlet	1.1	1.3
Exit (Behind Strut)	33.1	17.8
Exit (Between Strut)	26.5	14.5

Between the struts (Figure 11 – top), however, is a poor agreement between experimental and computational results. The computational velocity profile is shifted towards the center of the annulus, while the magnitudes are accurate within 3%. The minimum turbulence intensity occurs at the location of maximum velocity for both the experiment and computation, however the under prediction in high velocity regions is exaggerated between the struts. Again, this leads to the conclusion that the k-ε model is incorrectly dissipating the strut wakes, therefore dissipating turbulence between the struts. These results also reiterate the fact that the axial velocity fluctuations (u_{rms}) are the dominating factor in the shape of the turbulence intensity curve, as the trends of an isotropically derived quantity and the anisotropic k-ε turbulence are similar.

It was observed that the flow between the struts creates a velocity profile along the inner annulus that is analogous to the outer annulus. This trend is not seen directly downstream of the struts, as the flow tends to prefer the inner annulus. This is due to a small separation zone on the outer annulus of the diffuser just behind the struts. The geometric diffusion on the outer annulus causes this small separation, while the inner annulus which remains straight has a less significant separation zone. This outer annulus separation zone causes the bulk flow to shift closer to the inner annulus, resulting in a higher velocity. This effect proved to be true by analyzing the computational model.

The performance of the diffuser with no ECB (free discharge condition) was also calculated both experimentally and computationally and shown in Figure 12. It is observed that the computation slightly over predicts the pressure recovery through the diffuser in the low X/L range (maximum difference in Cp of 0.09); however the total amount pressure recovered by the diffuser was within 2% between the computation and the experimental results.

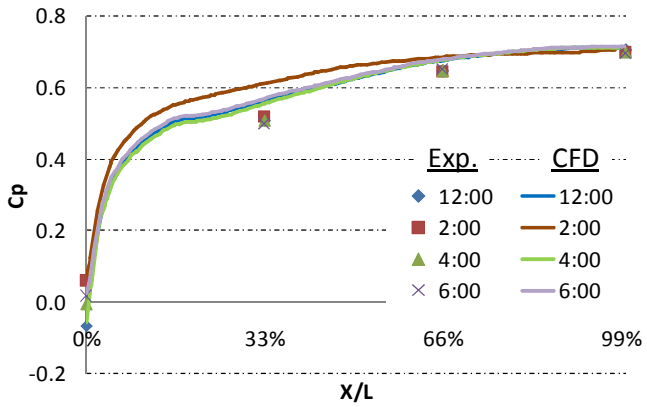

Figure 12 – Pressure recovery along the outer annulus of the diffuser with no ECB attached

This is caused by an under prediction of the separation on the outer annulus of the diffuser. The reason why the Cp value is not symmetric is due to the fact that the inherent behavior of the diffuser by itself is naturally unsteady. The steady RANS model will not model the unsteadiness of the system, therefore the model will not fully converge to a single solution. The "converged" model has oscillatory residuals which validates the assumption of unsteadiness in the model. The separation within the diffuser moves around slightly at each iteration, which causes a difference in Cp values at certain locations. If an unsteady RANS were to be time averaged over a long period of time, these Cp curves would fall on top of each other due to the symmetry. Figure 13 shows an example of this asymmetric separation bubble within the diffuser. The white zones are reversed flow areas within the diffuser. While this solution may not be physically accurate (due to the reasons stated above) it is an example of a situation in which a symmetric model with symmetric boundary conditions can cause variations in static pressure at the inlet of the diffuser. It should be noted that while the diffuser alone has a moving separation zone, the full computational domain (including the ECB) did not have an unsteady nature, and converged to a single solution. The backpressure effects of the ECB forced separation in specific locations, killing the unsteady oscillations of the separation zone.

By comparing these experimental results with the computational results, it is apparent that the trends were captured correctly. The static pressure is over predicted along the diffuser due to the under prediction of separation, however this effect will be addressed further later. The experimental results describing the inlet velocity profile to the diffuser gives confidence to the inlet boundary condition used in the computational model as a constant mass flow rate, thus a flat velocity profile. These results give enough confidence in the understanding of the computational model to continue with the main study of this paper, which is the performance of the entire exhaust system.

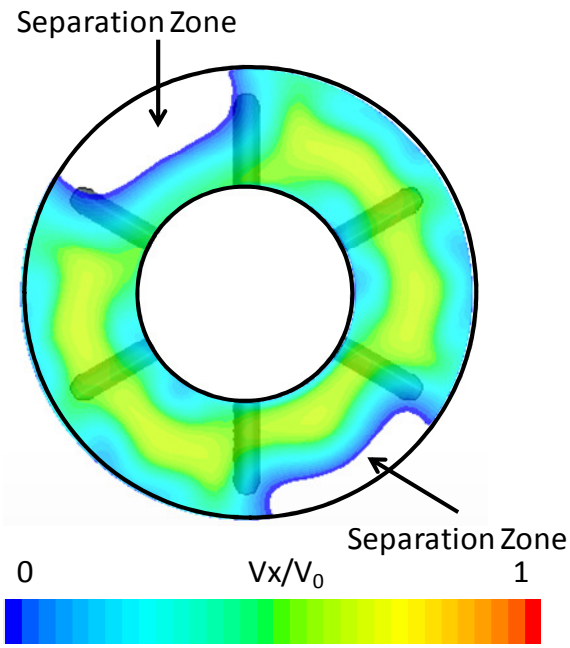

Figure 13 – Axial velocity profile at the exit of the diffuser under a free exit condition showing the asymmetric separation zones

Figure 14 shows the static pressure recovery through the diffuser while the ECB was attached. Much like the other common turbulence models described in [19] under similar adverse pressure gradient systems, the pressure recovery of the realizable k-ε turbulence model is over predicted.

As stated before, the separation within the diffuser with a free exit condition was under predicted, resulting in a slight increase in Cp along the outer wall. This effect is exacerbated when the ECB is introduced into the system. It is clear that the computational model is severely over predicting the pressure recovery (up to 15% over prediction at X/L=33%), leading to the conclusion that the separation phenomenon along the outer wall is under predicted. It is observed that the 12:00 and 2:00 locations show a local static pressure drop near the exit of the diffuser, which is counterintuitive for a diffuser system. However, due to the bulk flow within the ECB, it is observed that the flow exiting the diffuser in the 12:00 location is being turned 90 degrees prior to the exit of the diffuser. This causes flow separation off the inner annulus, and reattachment on the outer annulus and local acceleration around the bend (shown later in Figure 18).

It can also be observed that the overall pressure recovery of the diffuser does not change significantly with a change in ECB length.

Case 2 recovered only 2.5% more pressure than Case 1 (both experimentally and computationally) while Case 3 recovered 4% more experimentally (3% computationally). It is also observed that the 6:00 location recovers 7.5% more pressure over the first 50% of the diffuser length than the average. The lack of pressure recovery in the second half of the diffuser at the 6:00 location is due to separated flow along the outer annulus, which was confirmed by the computational results.

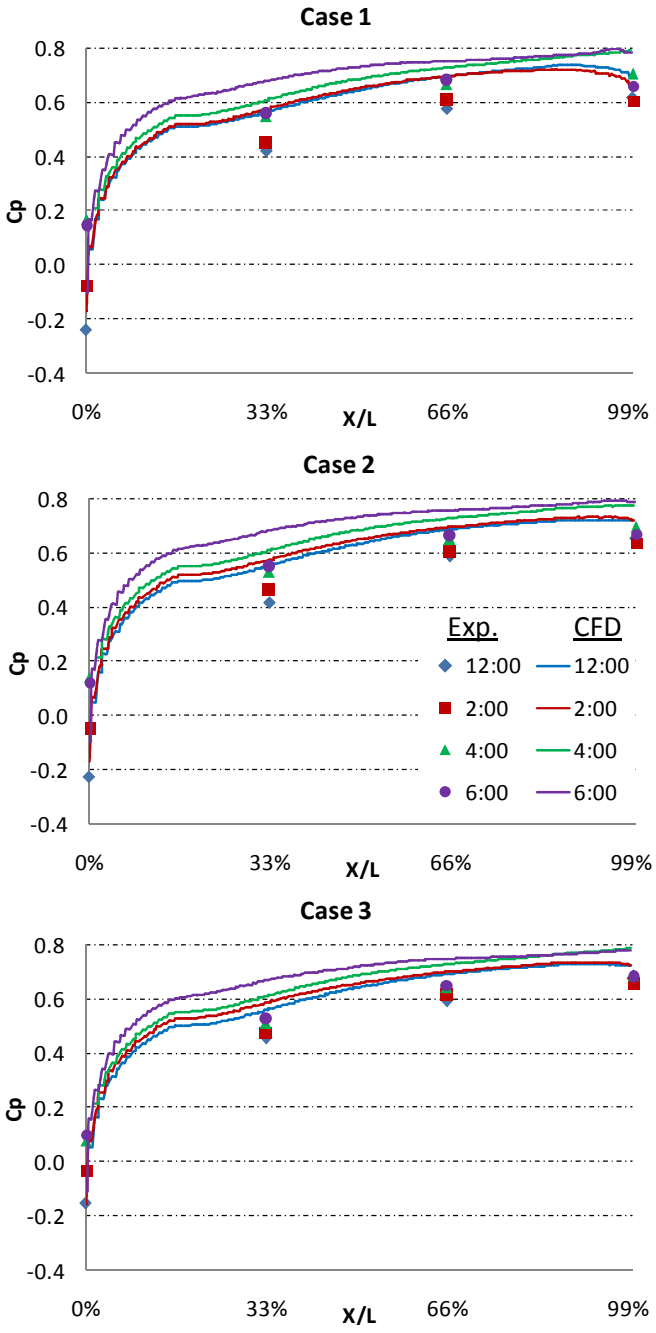

Figure 14 – Pressure recovery coefficient reported for Case 1, 2, and 3 (top, middle, bottom respectively).

In order to investigate the circumferential variations in pressure recovery, the maximum circumferential variation in Cp at the inlet and exit are tabulated in Table 4. It is observed that the addition of an ECB creates a drastic change in the circumferential pressure variations at the inlet of the diffuser.

Case 1 has a maximum variation at the inlet of over 300% of the case with no ECB attached. As the ECB length is increased, this inlet variation decreases by 10% in Case 2, and by 40% in Case 3.

Table 4 –Maximum variations in pressure recovery

	Maximum Circumferential Variation in Cp			
	X/L=0%		X/L=100%	
	Exp.	CFD.	Exp.	CFD.
No ECB	0.13	0.13	0.01	0
Case 1	0.41	0.38	0.10	0.13
Case 2	0.37	0.38	0.06	0.07
Case 3	0.25	0.37	0.03	0.06

The computational results correctly captured the 300% increase when the ECB was introduced to the system; however the variations remained constant through each of the cases. The exit of the diffuser had no variation experimentally under a free discharge condition, matched by the CFD due to the constant pressure exit boundary condition. When the ECB was introduced, the maximum difference circumferentially was 14% of the total amount of pressure recovered experimentally. This variation is halved in Case 2, and halved once more in Case 3. The computational model predicts a 5% higher circumferential variation in Case 1, however this variation halves in Case 2. These results show that the ECB has a significant impact on the pressure recovery of the diffuser. The increased static pressure variations at the diffuser inlet (with the ECB attached to the system) are caused by the pressure distribution in the ECB propagating through the diffuser.

Within the ECB, the 6:00 location has a higher pressure than the 12:00 location; this can be seen in Figure 16 by looking at the "Front" of Case 1. This exit condition for the diffuser propagates all the way down to the inlet of the diffuser, as the flow prefers the path of least resistance (i.e. towards the 12:00 location). A decreased resistance along the 12:00 location due to a reduction in back pressure will increase the mass flux in this area, which in turn causes a lower static pressure at the inlet of the diffuser. The opposite of this is true for the 6:00 location, which has an increased resistance due to an increase in back pressure, reducing mass flux and in turn causing a high static pressure at the inlet. The 2:00 and 4:00 locations show a gradual change in static pressure that validates this conclusion. This effect is seen both experimentally and computationally when the ECB was introduced into the system.

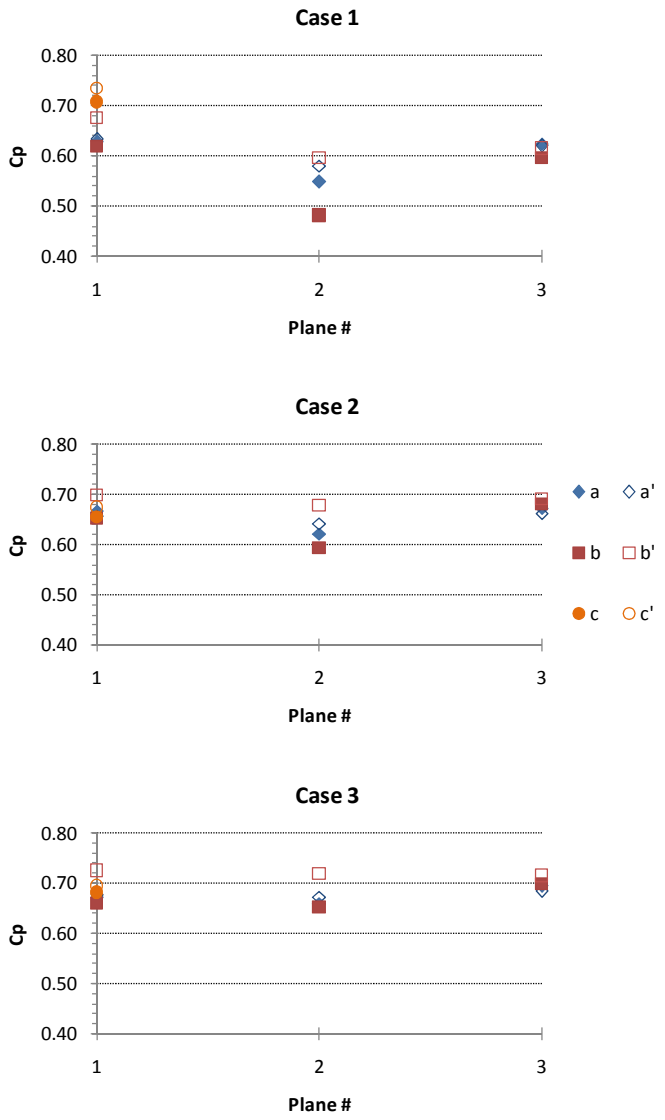

Figure 15 – Pressure recovery trends presented for the ECB for Case 1, 2, and 3 (top, middle, bottom respectively)

ECB Performance

Figure 15 shows the static pressure along the front and back walls of the ECB for each geometry. It is observed that the static pressure is on average 6.5% higher on the back wall than on the front wall for Case 1, and 3.5% higher in Case 2 and 3. This is expected due to the impingement effect from the diffuser exit. It can also be determined that the static pressure recovery is highest at the centerline of the ECB (along plane 1), then as the radial position increases from the centerline to the diffuser wall (plane 2) the pressure recovery drops by 17% in Case 1 then increases by 10% when we approach the wall (plane 3).

It is also noted that as the ECB length is increased from the case 1 to Case 2, the pressure recovery at the

centerline (plane 1) remains constant. However, as the radial placement increases from plane 1 to plane 2, the pressure recovery increases significantly at each port, from an average Cp of 0.55 to 0.65 (an 18% increase) from Case 1 to Case 2. As the ECB length is increased further, this same general trend is apparent, however the increase in Cp is not as significant as the difference between Case 1 and Case 2 as the average Cp only increased by 5%. It is also observed that the variations between the front and back wall decrease from 6.5% in Case 1 to 3.5% in Case 2 and 3. This leads to the conclusion that the vortex cores have decreased in strength in the larger ECB cases (Case 2,3) when compared to Case 1. The increased geometric size of the ECB gives the vortices a chance to dissipate before exiting the ECB, while the small area in the baseline case tends to restrict the dissipation of these vortices.

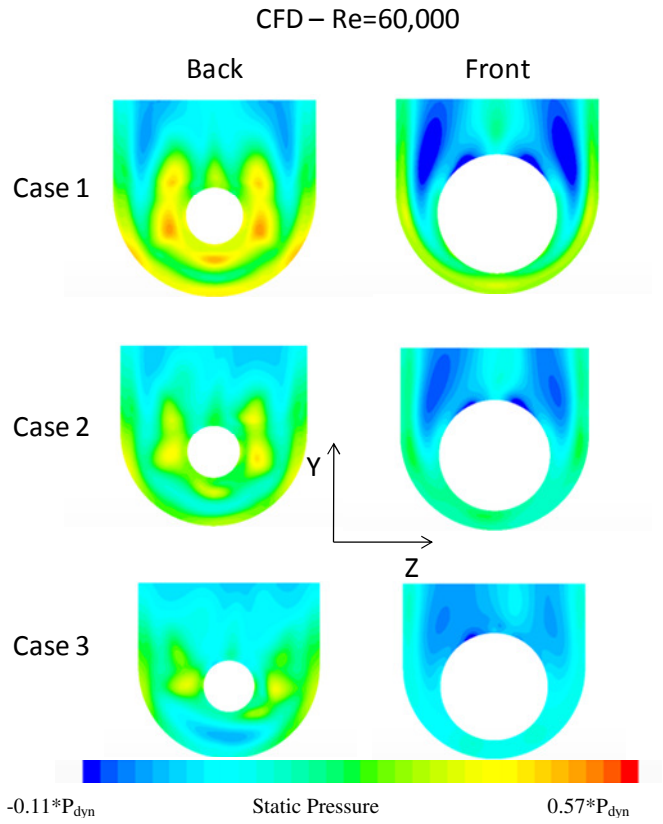

Figure 16 – ECB front and back wall static pressure distributions from the numerical solution (non-dimensionalized by inlet dynamic head)

From the computational results (Figure 16), these trends match very well. The centerline (plane 1) shows very little variations in the static pressure from bottom to top, while lines 2 and 3 have significant variations (refer to Figure 6 for coordinate system). The computational results also conclude that plane 2 has significantly lower pressures than the rest of the ECB on the front and back walls, especially near the exit of the ECB. This stems from the fact that the vortex cores are located very near to plane 2 in all cases, showing a low pressure zone along this plane. This pressure is slightly higher near the side walls, as Plane 3 is outside of the vortex core's low pressure zone, which is evident from the experimental results as well. This is due to the presence of two large vortices within the ECB, which are investigated in the next section. It should also be noted that the variations in static pressure at the ECB exit are extremely severe in case 1 (maximum difference of 22.5% between Plane 1 and 2), while case 3 has very minor variations (less than 3% difference between Plane 1 and 2). This leads to the conclusion that the vortex cores are weaker in Case 3, which is confirmed in the next section.

ECB Exit Plane Profiles

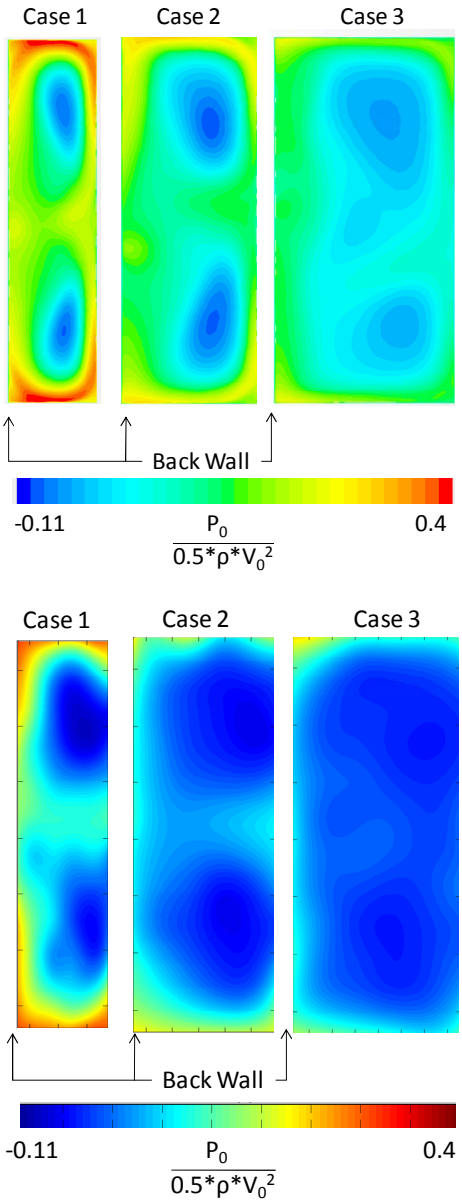

Figure 17 – gage total pressure profiles at the ECB exit plane from the numerical solution (top) and the experimental results (bottom) (

A matrix of 72 locations at the ECB exit was measured with a Kiel probe to get a total pressure profile for each case. Figure 17 shows two significant low pressure regions at the exit of the ECB. These are due to the presence of two counter rotating vortices within the ECB. The intensity of these vortices decreases significantly as the ECB length is increased from case 1 to case 3 in both the experimental and computational cases.

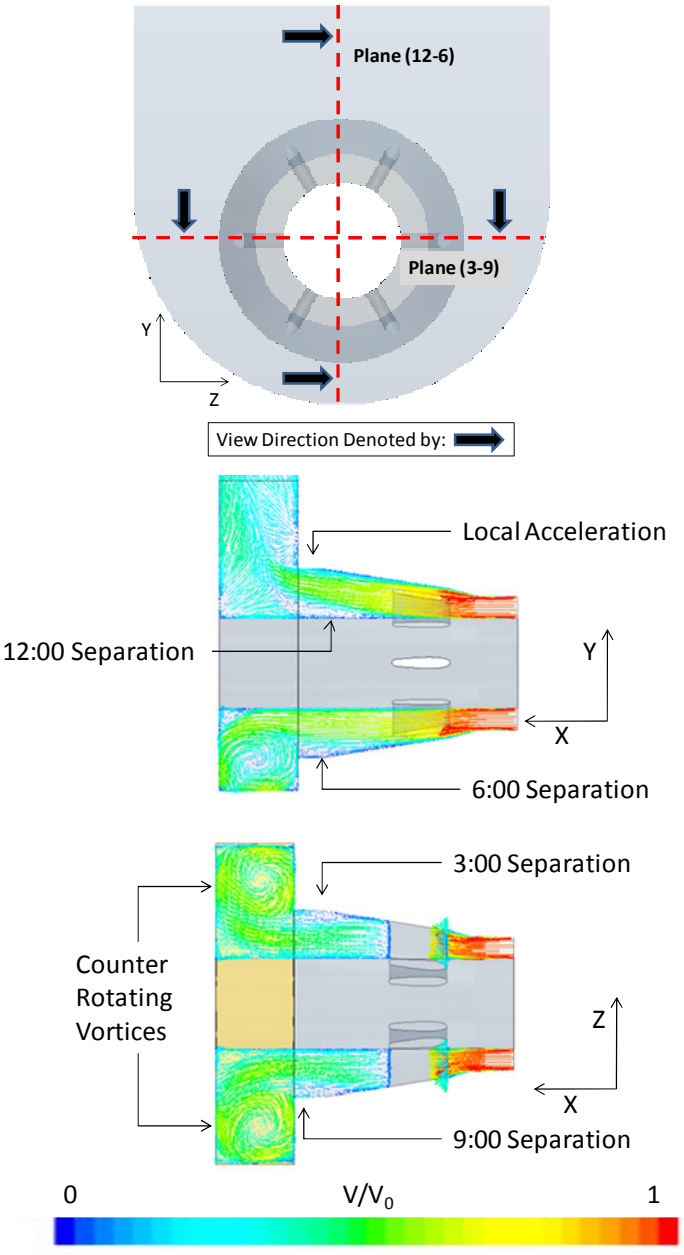

Figure 18 – Velocity vectors showing separation within the diffuser, and counter rotating vortices in the ECB for the 12:00 – 6:00 plane (mid) and the 3:00 – 9:00 plane (bottom) (non-dimensionalized by the diffuser inlet velocity)

The experimental result and the computational result agree quite well for the profile shape, the locations of the vortex cores, and the total pressure at the core. However, the computation tends to predict slightly higher pressures around the vortex cores. These counter rotating vortices originate from the exiting flow from the diffuser impinging onto the back wall of the ECB and turning back towards the diffuser. This creates a strong vortex at the exit of the diffuser at the 6:00 location, which is then pushed up and out of the ECB by the bulk flow motion. The combination of these two effects creates two counter rotating vortices on each side of the inner annulus that span the entire length of the ECB. This is illustrated in Figure 18. It can also be seen that at the 3:00, 6:00, and 9:00 locations, this vortex forces separation at the exit of the diffuser due to the flow traveling towards the inner annulus, thus lifting the flow off the walls of the diffuser. The opposite effect is true for the 12:00 location, as the flow is traveling towards the outer annulus causing separation off the inner annulus, and a local acceleration at the outer annulus exit. This confirms the pressure recovery trends presented earlier in this study.

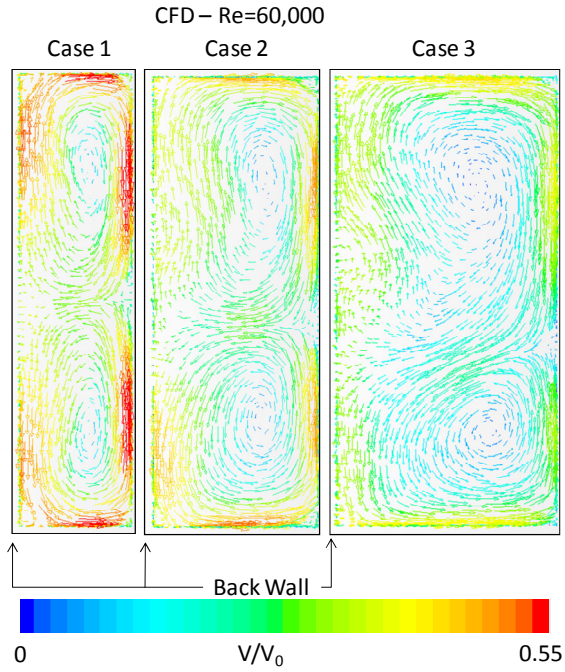

Figure 19 – Computational results for the velocity vectors at the ECB exit plane. (view from downstream) (non-dimensionalized by the diffuser inlet velocity)

Figure 19 shows the velocity vectors at the ECB exit plane. These vectors confirm that the vortices are still present at the exit of the ECB, and the strength of these vortices are heavily dependent on the ECB length. Case 1 shows a very high rotational speed around the vortex cores (approximately 50% of the diffuser inlet velocity). When the ECB length is increased by 100% in Case 3, this rotational speed decreases significantly (approximately 20% of the diffuser inlet velocity). This

phenomenon agrees with the experimental conclusion that the vortices weaken as the ECB length is increased.

System Pressure Loss

The static pressure drop/recovery and total pressure loss coefficients are presented in Figure 20. It is observed that the vast majority of the pressure recovery occurs within the diffuser. It is also apparent that there is a small amount of static pressure lost within the ECB, despite the fact that it acts as the second diffuser in the system. These losses decrease as the ECB length is increased. The computational results tend to over predict the pressure recovery through the diffuser however it agrees very well with the ECB exit location. The experimental results show that the ECB tends to recover more pressure as the ECB length is increased. Once again, this is due to the weakening of the two counter rotating vortices within the ECB. The computational domain accurately represents the static pressure recovery through the system in trends and magnitudes.

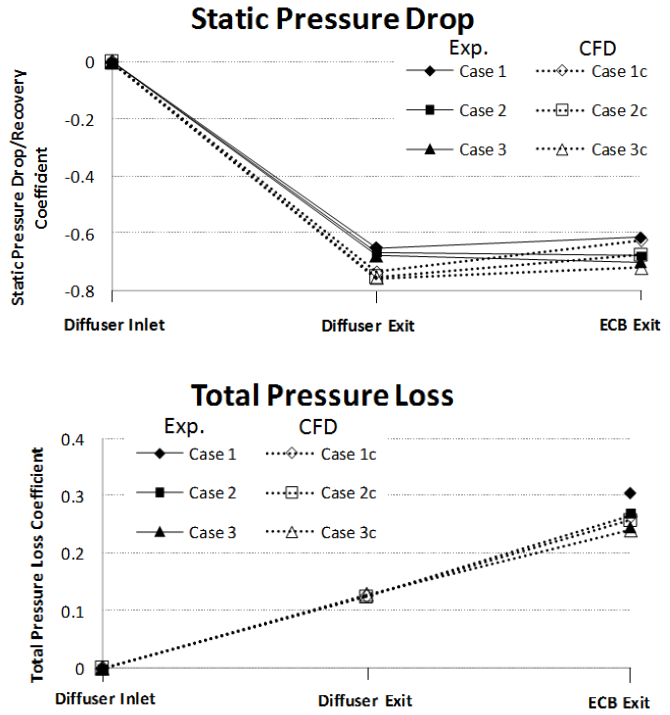

Figure 20 – Static pressure drop and total pressure loss coefficients for experimental and computational models

The total pressure loss coefficient shows that the diffuser has an equal amount of losses through each case. The static pressure recovery is affected by the ECB, however the total pressure losses are not. The ECB itself, however, has significant differences per case. Case 1 shows the highest total pressure losses, and Case 3 shows the lowest both experimentally and computationally.

Case 3 shows a total pressure loss coefficient reduction from Case 1 of 19% experimentally and 10% computationally. Once again this difference stems from the strength of the dual vortices within the ECB. The computational domain shows an under prediction for Case 2 and 3 of 5% and 3% respectively for the system total pressure loss, however Case 1 shows a significant under prediction of the total losses at 13%. This is mainly due to the fact that the computational domain does not accurately model the turbulent dissipation within the vortices in the ECB, nor does it capture all of the eddies and turbulent mixing which contribute to the losses.

CONCLUSIONS

A typical gas turbine exhaust system was analyzed in this study under various ECB lengths and compared with a 3-dimensional RANS method with a realizable k-ε turbulence model. The conclusions of this study are as follows:

- The vortices within the ECB decrease in strength as the ECB length is increased from Case 1 to Case 3.
- The flow structure of the diffuser is affected by the presence of the ECB. The recirculation off the back wall forces separation on the outer annulus of the diffuser along the 3:00, 6:00, and 9:00 locations and forces separation off the inner annulus at the 12:00 location. The high pressure at the exit of the diffuser at the 6:00 location shifts the flow towards the 12:00 location. This effect propagates back to the diffuser inlet, causing circumferential pressure variations.
- The total pressure losses through the entire exhaust diffuser system decreased as the ECB length was increased. This is due to the weakening of the counter rotating vortex pair.
- The 3-dimensional RANS method with realizable k-ε turbulence model accurately depicts the trends of this complex adverse pressure gradient exhaust system. The computational model tends to under predict separation and over predict the pressure recovery through the diffuser, however the total pressure losses through the system for each case were within 5% for Case 2 and 3. This study has shown that this computational model is an important tool which can be used to successfully analyze designs for the gas turbine exhaust diffuser.

ACKNOWLEDGEMENTS

The authors would like to acknowledge Jason Kopko, Barry Brown, Tony Malandra, and Alexander Beeck for their support on this project, and the permission to publish the results. The authors acknowledge the support from the Florida Center for Advanced AeroPropulsion (FCAAP). This work was performed at and with the support from students and staff of the Siemens Energy Center – a research laboratory at the University of Central Florida made possible through funds from Siemens Energy. The authors also acknowledge the support for STAR-CCM+ and Dr. Rahan Guha for the permission to use the Ariel Cluster.

REFERENCES

[1] Bottenheim, S., Birk, A.M., Poirier, D.J. "The Effect of an entraining diffuser on the performance of circular-to-slot exhaust ducts with a 90 degree bend". ASME Turbo Expo 2006. GT2006-90017

[2] Ubertini, S., Desideri, U., "Experimental Performance analysis of an annular diffuser with and without struts" Journal of Experimental Thermal and Fluid Science, 2000, Vol 22, pp 183-195

[3] Sultanian, B.K., Nagao, S., Sakamoto, T., "Experimental and Three-Dimensional CFD Investigation in a Gas Turbine Exhaust System" J. Eng. Gas Turbines Power, April 1999, Volume 121, Issue 2, pp 364-375

[4] Hirschmann, A., Volkmer, S., Schatz, M., Finzel, C., Casey, M., Montgomery, M., "Influence of the Total Pressure Profile on the Performance of Axial Gas Turbine Diffusers" ASME Turbo Expo 2010, Paper No. GT2010-22481

[5] Sultanian, B.K., and Mongia, H.C., 1986, "Fuel Nozzle Air Flow Modeling." AIAA-86-1667

[6] Hirsch, C., and Khodak, A.E., 1995, "Application of Different Turbulence Models for Duct Flow Simulation with Reduced and Full Navier-Stokes Equations." ASME Paper 95-GT-145

[7] El-Askary, W.A., Nasr, M., "Performance of a bend-diffuser system: Experimental and numerical studies" Journal of Computers & Fluids (2009) pp160-170.

[8] Ishizaka, K., Wakazono, S., Yuri, M., Takahashi, R., "CFD Studies of Industrial Gas Turbines Exhaust Diffusers" International Gas Turbine Congress 2003, November 2003, Paper No. IGTC2003Tokyo TS-026

[9] Vassillev, V., Irmisch, S., Abdel-Wahab, S., Granovskiy, A., "Impact of the Inflow Conditions on the Heavy-Duty Gas Turbine Exhaust Diffusers Performance" ASME Turbo Expo 2010, Paper No. GT2010-22840

[10] Cherry, E., Padilla, A., Elkins, C., Eaton, J. "Three-dimensional Velocity Measurements in Annular Diffuser Segments Including the Effects of Upstream Strut Wakes" Journal of Heat and Fluid Flow 2010 Vol 31, pp569-575

[11] Dunn, J.J., Ricklick, M., Kapat, J.S., "Flow Characterization of a Three-Dimensional Separated Annular Diffuser" IMECE2009, Paper No. IMECE2009-10533

[12] Pradeep, A. M., Roy B., Vaibhav, V., Srinuvasu, D., "Study of Gas Turbine Exhaust Diffuser Performance and its Enhancement by Shape Modifications" ASME Turbo Expo 2010, Paper No. GT2010-22088

[13] Wolf, S., and Johnston, J.P., 1969, "Effects of Nonuniform Inlet Velocity Profiles on Flow Regimes and Performance in Two-Dimensional Diffusers." ASME Journal of Basic Engineering, Sept., pp. 462-474

[14] Eckert, W.T., Mort, K.W., Jope, J. "Aerodynamic Design Guidelines and Computer Program for Estimation of Subsonic Wind Tunnel Performance" National Aeronautics and Space Administration Ames Research Center. NASA TN D-8243. Washington, DC. October 1976

[15] Kline, S., and McClintock, F., 1953, "Describing Uncertainties in Single-Sample Experiments," Mechanical Engineering, 75, pp. 3-7

[16] McKeon, B.J., Swanson, C.J., Zagarola, M.V. "Friction factors for smooth pipe flow" J. Fluid Mech. (2004). Vol 551, pp. 41-44

[17] Star-CCM, 2010, "Star-CCM+ Version 5.04", USA, CD-adapco

[18] Celik, I.B., Ghia, U., Roache, P.J., Freitas, C.J., Coleman, H., Raad, P.E., "Procedure for Estimation and Reporting of Uncertainty Due to Discretization in CFD Applications" J. of Fluids Engineering (2008). Vol 130

[19] El-Behery, S.M., Hamed, M.H., A Comparative study of turbulence models performance for separating flow in a planar asymmetric diffuser, *Computers & Fluids* (2011), doi: 10.1016/j.compfluid.2011.01.009

[20] Pope, Stephen. Turbulent Flows. Cambridge University Press: Library of Congress, 2000